Composites Science and Technology 83 (2013) 11–21

Contents lists available at SciVerse ScienceDirect

Composites Science and Technology

journal homepage: www.elsevier.com/locate/compscitech

Damage quantification in polymer composites using a hybrid NDT approach

Jefferson Cuadra [a], Prashanth A. Vanniamparambil [a], Kavan Hazeli [a], Ivan Bartoli [b], Antonios Kontsos [a,*]

[a] Mechanical Engineering & Mechanics Department, Drexel University, Philadelphia, PA, United States
[b] Civil, Architectural and Environmental Engineering Department, Drexel University, Philadelphia, PA, United States

ARTICLE INFO

Article history:
Received 15 October 2012
Received in revised form 10 March 2013
Accepted 17 April 2013
Available online 25 April 2013

Keywords:
A. Polymer–matrix composites (PMCs)
C. Damage mechanics
D. Non-destructive testing
D. Acoustic emission
Digital image correlation

ABSTRACT

Damage is an inherently dynamic and multi-scale process. Of interest herein is the monitoring and quantification of progressive damage accumulation in a newly developed glass fiber reinforced polymer composite subjected to both tensile and fatigue loading conditions. To achieve this goal, the potential of data fusion in structural damage detection, identification and remaining-life estimation is investigated by integrating heterogeneous monitoring techniques and extracting damage-specific information. Damage monitoring is achieved by the use of a hybrid non-destructive testing system relying on the combination of acoustic emission, digital image correlation and infrared thermography. Full-field strain and temperature differential maps reveal appearance and development of damage "hot spots" at prescribed strain/load increments that also correlate well with distinct changes in the recorded acoustic activity. The use of non-destructive and mechanical testing data further allows the quantification of the observed hysteretic fatigue behavior by providing measurements of the: (i) stiffness degradation, (ii) energy dissipation, and (iii) average strain as a function of fatigue cycles. Furthermore, analysis of the real time recorded acoustic activity indicates the existence of three characteristic stages of fatigue life that can be used to construct a framework for reliable remaining life-predictions.

1. Introduction

The emerging use of fiber reinforced polymer composites (FRPCs) in aerospace [1] and power generation applications [2], is justified by their exceptional combination of properties including high specific strength and stiffness [3]. However, more than three decades since their appearance, the widespread acceptance of FRPC as a reliable class of engineering materials remains an issue. The reasons for this observed hysteresis between development and application of FRPC can be traced primarily in the inability to effectively model and predict their performance and remaining life as a function of both applied load and evolving surrounding environment [4,5], as for example currently accomplished in the case of metal alloys [6]. The resulting uncertainty naturally increases the risk in using this material type and ultimately overweighs their comparative advantages as engineering materials.

Failure in laminated polymer composites is driven by various damage mechanisms including matrix cracking, fiber breakage, interfacial debonding, transverse ply cracking, and ply delamination [7]. The number, activation and interactions of these failure mechanisms is further heavily dependent on prior manufacturing and machining operations, that often result in defects and pre-damage conditions that ultimately affect the observed failure patterns [8,9]. In addition, the probable simultaneous activation of two or more of such failure mechanisms and their unpredictable evolution with applied loading, changing material states, and interactions with the overall structural design, create the need for the development of effective strategies for early detection of damage initiation, as well as subsequent tracking of its evolution and accumulation [10]. In this context, nondestructive testing (NDT) methods have proved invaluable both in understanding the complex behavior of FRPC and in monitoring their damage process. Recent NDT applications for damage monitoring of composites include the use of non contact optical methods [11–16], acoustic-based techniques [17–21], as well as electrical potential/resistance approaches [22,23]. In addition to NDT, other methods have been used for monitoring the degradation of properties and the bulk mechanical behavior of composites using standard metrological devices, such as extensometers and strain gages [10,24–27]. Although such efforts have had some success in characterizing the mechanical and damage behavior of composite materials, an integrated approach which could effectively and reliably track and quantify both damage initiation and subsequent damage evolution is needed [5,28,29].

* Corresponding author. Tel.: +1 215 895 2297; fax: +1 215 895 1478.
E-mail address: akontsos@coe.drexel.edu (A. Kontsos).

0266-3538/$ - see front matter © 2013 Elsevier Ltd. All rights reserved.
http://dx.doi.org/10.1016/j.compscitech.2013.04.013

This paper addresses the experimental procedure followed to obtain in situ cross-validated NDT data as a function of loading in uniaxial tensile and tension–tension fatigue tests. To this aim, digital image correlation (DIC), infrared thermography (IRT) and acoustic emission (AE) testing were used in parallel to quantify the damage process in Glass Fiber Reinforced Polymer (GFRP) composites intended for use in wind turbines.

2. Background

A robust monitoring system based on periodical, triggered or continuous inspections, should be capable of determining whether the current state of a material or structural component has deviated from its normal operational conditions, i.e. damaged. For this purpose, innovations in NDT technologies including both novel sensor platforms (e.g. embedded carbon nanotube networks [30] or fiber bragg sensors [31] in newly manufactured composites for on line structural assessment) and several advanced post-processing methods (e.g. the class of statistical pattern recognition (SPR) techniques [32]) have been reported. Data post-processing through information integration, a process frequently called "fusion", is either inherently built in the harvesting part of the system or is applied in post mortem. At the sensor level fusion has been achieved by novel platforms with multiphysics sensing capabilities (e.g. piezoelectricity plus strain) that collect in parallel independent information or implement acceptance criteria for hierarchical recordings based on switching and rejection protocols [33]. Fusion may also occur at the post-processing level in which heterogeneous sensing units provide inputs that are subsequently classified by the data acquisition system using intelligent schemes including machine learning [34], as well as neural/fuzzy/probabilistic networks [35,36], outlier analysis (OA) [37,38] and probability density estimations [39] to name a few.

The NDT monitoring approach in this paper is based on the use of three different techniques briefly described next for completeness that can provide complementary surface and volume information to describe damage initiation and development in composite materials and relate them to remaining life estimations. Specifically, AE is a promising technique to monitor developing damage in FRPC as it can track in real time both the activation and evolution of various damage mechanisms as a function of applied loading. AE refers to stress waves that are produced by the rapid release of energy caused by reversible/irreversible changes within the material. Previous work on AE focused on relating extracted features, such as counts and amplitude to damage as a function of e.g. the number of fatigue cycles [17,19,20]. Furthermore, Barre and Benzeggagh [40] correlated AE amplitude with SEM images to investigate the various damage mechanisms present in glass fiber composites. Additionally, spectral analysis has been used to differentiate the different damage mechanisms such as matrix cracking and fiber breakage [21]. Sause and Horn [41] developed a finite element model (FEM) to simulate the AE from targeted damage modes in carbon fiber reinforced composites and used the frequency content of the numerically produced AE signals to infer on ways to effectively detect damage experimentally. However, material type, geometry and damage mode interaction complexities in fiber reinforced composites, and additional uncertainties introduced by the AE sensors have revealed severe difficulties in the identification of damage modes using conventional, "feature-based" AE monitoring. To address such difficulties, SPR algorithms based on both unsupervised and supervised modes of learning have been implemented with the goal to correlate mathematically defined clusters of AE data with deformation and damage mechanisms [42]. Additional difficulties even in such advanced post-processing techniques have been reported, which create the need for cross-validation of recorded AE information with both other NDT information and mechanical data during testing, as described in this article.

DIC is a non-contact optical metrology technique capable of measuring full-field in and out of plane displacements and computing in-plane strains on the surface of a specimen undergoing deformation [43,44]. The technique relies on measurements of surface deformation by comparing an original (reference) configuration with subsequent deformed states through tracking contrast changes in light intensity fields typically achieved by applying a speckle pattern on the tested sample. This emerging optical method has been successfully employed to investigate material characterization and failure mechanisms of FRPC subjected to monotonic and cyclic loadings [11–16]. The DIC method has also been employed to obtain better understanding of the micromechanical behavior of FRPC by analyzing strain distributions and associated fracture surfaces [13,14,16].

Infrared imaging which allows real-time tracking of surface temperatures, have permitted thermography techniques (including active and passive) to grow as reliable and successful methods for both material inspection and characterization. Measuring the infrared radiation emitted by samples subjected to mechanical loading has provided damage accumulation monitoring by means of heat dissipation measurements [11,19,45–50]. Ghorbel et al. [46] for example studied the temperature increase of glass reinforced polyamide in a monotonic tensile test during yielding and necking. Toubal et al. [47] analyzed damage evolution in notched carbon fiber reinforced epoxy samples based on calculations of residual stiffness degradation, which was additionally compared to average surface temperature fluctuations as a function of the number of fatigue cycles. In addition, Broughton [11] provided the inverse relationship between normalized residual stiffness and surface temperature using the fatigue cycles as a correlation parameter for E-glass epoxy laminates. A similar trend was observed and measured by Reis et al. [19] in conjunction with AE features in pristine glass fiber reinforced polypropylene samples.

3. Experimental setup

3.1. Hybrid NDT system

The hybrid NDT system used for mechanical tests is shown in Fig. 1a; the AE part consisted of a four-channel DiSP system (Physical Acoustics); two piezoelectric transducers (Pico) were mounted on the specimen as shown in Fig. 1b using cyanoacrylate adhesive. The piezoelectric transducers had an operating frequency range of 200–750 kHz with a peak frequency at 500 kHz. The received signals were amplified using 2/4/6-AST preamplifiers with a uniform gain of 40 dB, while threshold values of 65 and 60 dB were used for the tension and fatigue test, respectively. These rather high threshold values minimized the recordings of unwanted noise, such as mechanical vibrations introduced by the MTS testing machine. The recorded signals were band-pass filtered in a frequency range of 100 kHz–2 MHz and the pick definition time, hit definition time and hit lockout time settings used were 40, 80 and 300 μs, respectively. Before testing, lead break tests were carried out to determine the sensitivity of the sensors, calibrate the system and calculate a surface wave speed of 12,000 m/s. The use of two sensors further permitted linear location source detection during testing.

A GOM ARAMIS 3D 5 megapixel DIC system with a peak image acquisition rate of 30 frames/s (fps) was utilized to record full field strain maps for the duration of the test. A $65 \times 55\ mm^2$ (2400×2100 pixels) field of view (FOV) was employed. 3D surface deformations were obtained through triangulation of the two

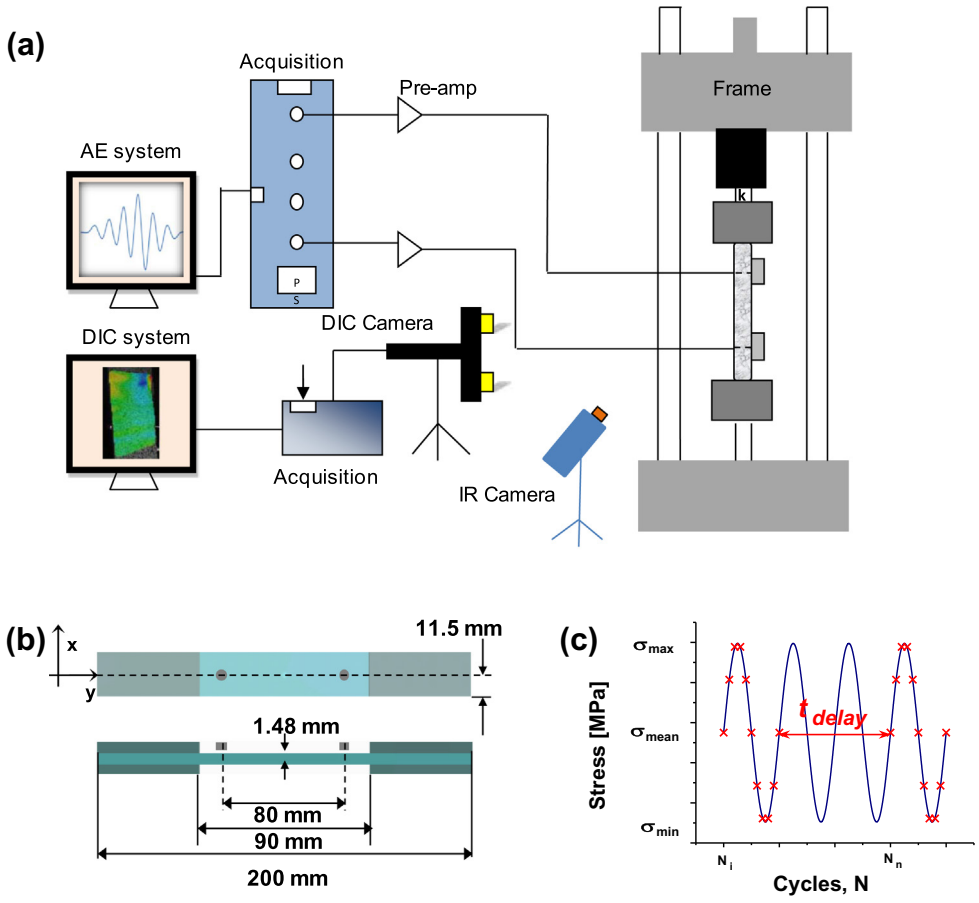

Fig. 1. (a) Hybrid NDT experimental setup; (b) material specimen geometry; and (c) custom DIC image acquisition for the imposed cyclic sinusoidal loading profile.

camera lenses. A stochastic speckle pattern was applied on the front surface to create a vivid surface light contrast and to track the deformation process. DIC images were captured at a rate of 1 fps during the tensile tests. In the fatigue tests, the DIC system was programmed to record images at 11 fps using an in-house-developed script, which triggered the DIC cameras at specific time instances that corresponded to target force values (marked with X in Fig. 1c). The strain uncertainty for DIC measurements reported in this article was ±150 μm/m, achieved by a facet size of 25 × 25 pixels, a step size of 12 pixels and 52% overlap.

Infrared thermography was performed using a Fluke Ti55 IR FlexCam camera system operating in the 8–14 μm range. A thermal emissivity of 0.75 with an acquisition rate of 0.2 fps for both the tensile and fatigue tests was utilized. The focal plane array pixel format was 320 × 256 pixels for a FOV of 172 × 230 mm^2. The background temperature was set to 70 °F and the accuracy of the system was ±2 °C for a temperature from −25 °C to 100 °C.

3.2. Material and loading specifications

The composite material tested was a glass fiber reinforced epoxy laminate consisting of E-glass fibers and epoxy resin with dimensions 200 mm × 23mm × 1.48 mm. The material had a stacking sequence of [0/90/90/0] with a fiber volume fraction of 54%. The GFRP specimens were tested both in displacement-controlled tension and force-controlled tension–tension fatigue with a sinusoidal profile using a MTS servohydraulic testing machine. Tensile tests were carried out at a 2 mm/min displacement rate in accordance with ASTM D3039. Fatigue loads were selected based on the ultimate tensile strength measured in the tensile tests. The fatigue tests were carried out at a frequency rate of 3 Hz with a minimum to maximum stress ratio (R-value) of 0.1.

4. Results and discussion

4.1. Tensile testing

Fig. 2a presents the obtained stress–strain (σ–ε) behavior correlated with the AE amplitude distribution and average temperature differential evolution. Corresponding full field DIC and IRT results at marked locations along the σ–ε curve are shown in Fig. 2b. Strain values in the σ–ε curve were computed by averaging full field strain measurements in the longitudinal direction. The temperature differential values were calculated by the ratio of the absolute temperature difference over the initial temperature. It is clear in Fig. 2a that both the temperature differential and scatter AE amplitude increase significantly as the stress increases. At point marked as 2, the stress suddenly drops and a slight visual macroscopic damage could be detected as shown in the related top raw DIC image in Fig. 2c, strongly indicating sub-surface damage initiation. Note that such small stress drops are typically referred to as 'pop-ins' [51]. The corresponding average strain at point 2 was 1.8%. Both AE and IRT present distinct increases in their activity exactly at this point, with AE emissions demonstrating a large increase in both their event density and amplitude, while a subsequent decrease was observed past point 2.

The thermography measurements showed a large, sudden and steady increase in the temperature differential at point 2. Interestingly, both the full field longitudinal strain and temperature differential values started to show "hot spots" at the left side of the

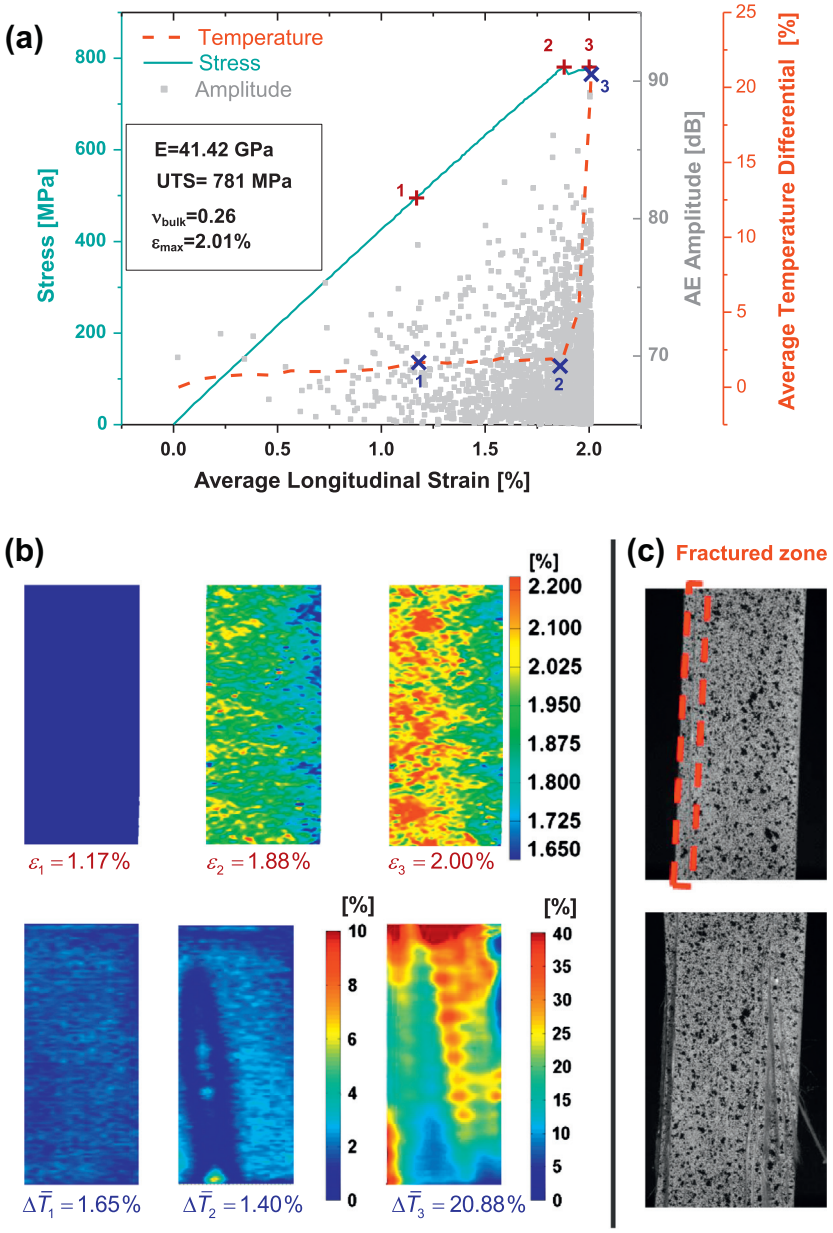

Fig. 2. (a) Measured tensile stress versus strain curves correlated with the distribution of real-time extracted amplitude of AE events and computed (in post mortem) average temperature differential values; (b) full field longitudinal strain (top) and temperature differential (bottom) maps; and (c) "raw" optical images recorded by the DIC system showing the specimen's surface at marked points 2 and 3, respectively in the stress–strain curve.

specimen, although no critical surface damage was observed. It is further interesting to note, that although at this load increment full field DIC data show rather fuzzy trends, the IRT results clearly mark the formation of a region at the left side of the specimen where incipient damage actually occurred, as shown in the second raw DIC image (bottom) in Fig. 2c. After the load drop at point 2, the stress started to increase again until point 3 where final fracture occurred. During this second, the average temperature differential continued to increase with an impressive ~18% rise for a short load increase period. This increase can be clearly correlated to the full field temperature differential, which shows high concentrations on the initial and final fracture zone, while the AE activity presented a second sudden rise in both event density and corresponding AE amplitude.

Fig. 3 presents further DIC results that correspond to the tensile tests in Fig. 2. Specifically, the average transversal strain (ε_x) in Fig. 3a (left) increased almost linearly with respect to the average longitudinal strain, for almost the entire duration of the test indicating linear behavior. However, after point 2, a nonlinearity was observed associated with critical failure damage formation described in Fig. 2. Corresponding local Poisson's ratio (PR) maps were computed based on full field longitudinal and transverse strains. At point 1, spots corresponding to relatively high PR values appear to form along the loading direction and can be compared to the GFRP constituents PR values ($\nu_{fiber} = 0.23$ and $\nu_{matrix} = 0.4$). These high values can be attributed to the increased transverse strain sustained by the matrix. At point 2, additional spots of lower PR values can be seen which could be related to matrix cracking and/or debonding in the specimen, resulting in the fibers carrying load. Furthermore, at point 3, the initial high PR spots seemed connected in a way that correlates well with the location and shape of the observed final fracture, indicating an interesting correlation

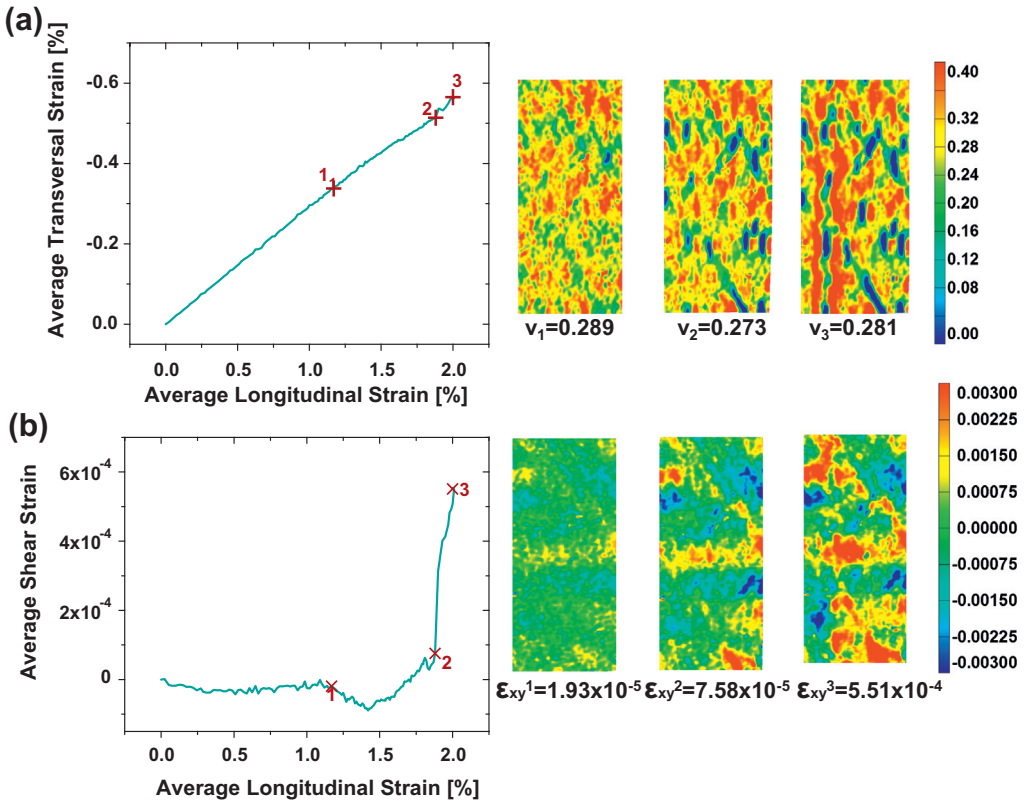

Fig. 3. (a) Average transversal strain as a function of imposed longitudinal strain and corresponding local Poisson's ratio maps computed by using recorded DIC data and (b) average shear strains versus longitudinal strain and related full field shear strain values.

between a locally resolved mechanical parameter only possible to be measured by a technique such as DIC, and occurring damage.

A possible method of evaluating the matrix–fiber bonding is by measuring the shear strain [29,52]. Fig. 3b shows the average shear strain (ε_{xy}) computed by DIC, as a function of the longitudinal strain. Interestingly, the slope of the shear strain changes significantly at point 1 (ε_y = 1.4% strain), as well as past point 2 (ε_y = 1.8% strain). While the average shear strain was found to increase for longitudinal strain values between 1.4% and 1.8%, it rapidly increased thereafter. Based on these findings, it can be suggested that the slope change at 1.4% strain could probably be associated with the initiation possibly of interfacial failure, while the significant increase of the shear strain at 1.8% can be related to the final stages of damage development. These remarks are further supported by the full-field shear strain visualizations also presented in Fig. 3b, which indicate the appearance and evolution of permanent concentrations, associated with significant strain values in regions related to the final fracture location shown in Fig. 2c.

To correlate the recorded AE results with both mechanical data and evolving damage in the material, the σ–ε curve versus the cumulative AE energy is plotted in Fig. 4a and versus the number of AE counts in Fig. 4b. The AE energy remained nearly constant initially and presented a significant jump at 1.8% strain level corresponding to the stress drop in the σ–ε curve, which can also be associated with the shear strain changes. Past 1.8% strain level, the AE energy continued to increase indicating severe source activity. Similarly, it can be seen at and past this strain level in Fig. 4b where both the number and density of counts increased significantly, offering additional evidence on the evolution of damage in the composite specimen.

Furthermore, unsupervised SPR analysis was performed to classify the recorded AE signals from the tensile tests. Four AE features were used as descriptors in this clustering methodology, namely, counts to peak, decay angle, absolute energy and peak frequency [42]. Based on previous work by the authors, the max–min distance algorithm was employed to remove any noise recorded during the test; and a complete link clustering algorithm with the selected four features was performed. The features were normalized and were found to have a correlation level less than 0.3, which is acceptable for clustering. The classification procedure was evaluated using the R and τ criteria, which yielded the case of 2 classes as optimum [42].

In Fig. 5a, the evolution of the absolute energy of the AE signals in each of the identified classes as a function of the average longitudinal strain is plotted. Class 0 appears to be active throughout the test with a noticeable change in slope at 1.4%; moreover, a distinct sharp increase at 1.8% in agreement with the results presented previously at point 2. Class 1 appears to be almost idle up to about 1.6%, where starts increasing with a slower rate compared to Class 0. To further investigate the properties of the identified clusters, the rise-time of the AE signals for each class is plotted against peak frequencies (Fig. 5b). Interestingly, class 0 AE signals seem to be linked with higher rise-time and lower peak frequency values which has been associated earlier in literature to matrix-dominated failure in composites (Fig. 6c), whereas class 1 comprises AE activity with relatively lower rise time and higher frequencies typical for fiber-dominated failure processes (Fig. 6a and b).

The weighted spectral content of the signals in each class was further analyzed using a Fast Fourier Transform (FFT) algorithm using the formula given in the following equation:

$$W_{FFT} = \frac{\sum_{i=0}^{N} XFFT_i}{N} \quad (1)$$

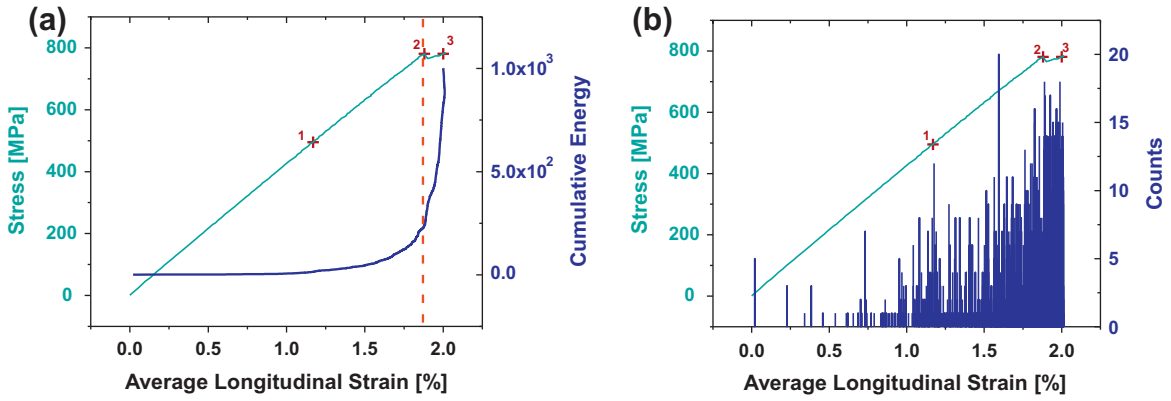

Fig. 4. Stress–strain correlation with (a) cumulative AE energy and (b) AE counts.

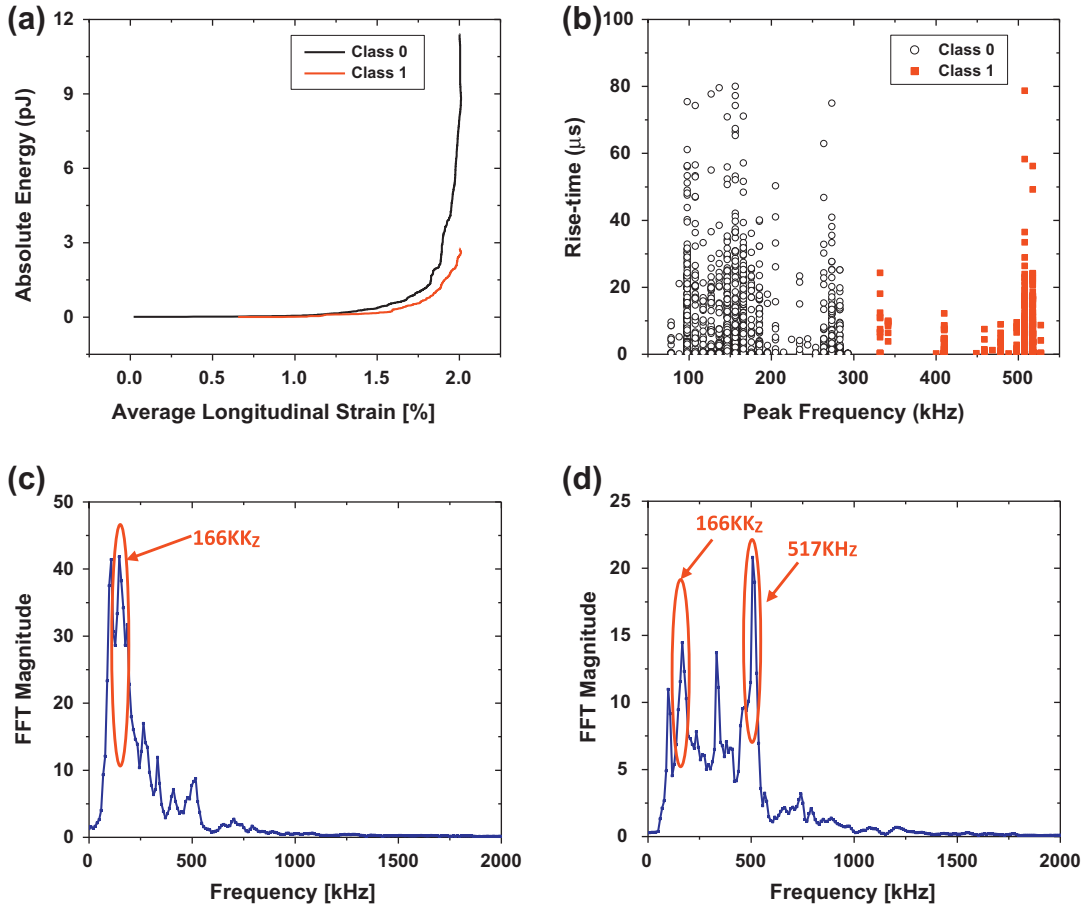

Fig. 5. SPR analysis: (a) Evolution of absolute energy with strain; (b) rise-time versus peak frequency; (c) weighted FFT of several signals in class 0; and (d) weighted FFT of several signals in class 1.

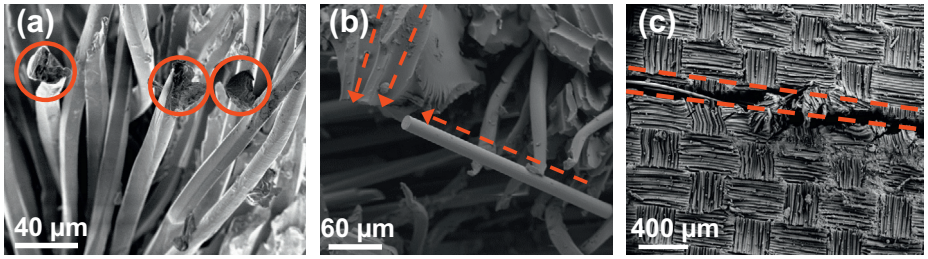

Fig. 6. SEM images of characteristics failure modes: (a) fiber breakage, (b) fiber pullout, and (c) matrix cracking.

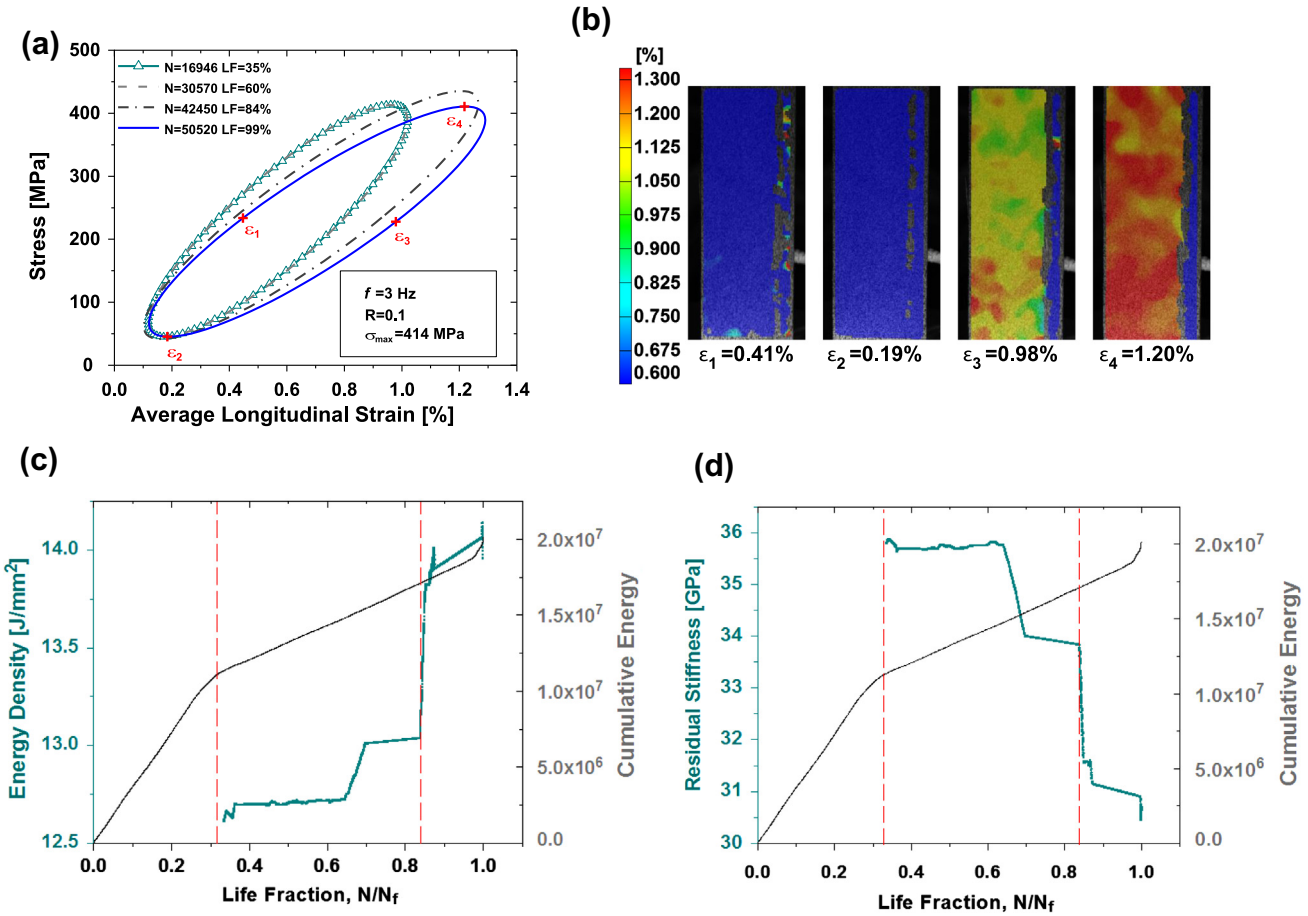

Fig. 7. (a) Representative fatigue stress–strain loops and (b) full field stain maps at marked locations 1–4 at LF = 99%. (c) Energy density and (d) residual stiffness compared to cumulative AE energy and versus normalized fatigue life.

where X_{FFT} is the *FFT* of a signal belonging to a particular class and N is the total number of signals. The results are shown in Fig. 5c and d for each class. The peak frequencies of class 0 and 1 lie around 166 kHz and 517 kHz respectively, while it is interesting to note that the 166 kHz peak of class 0 also appears in class 1 which correlates well with the absolute energy results in Fig. 5a. AE events with a dominant frequency <300 kHz have been associated to matrix cracking (Fig. 6c), fiber pullout (Fig. 6b) and fiber debonding (Fig. 6a), while events with >300 kHz peak frequencies typically correlate well with the fiber breakage dominated stage of failure in composites [53–55]. Such damage modes were revealed by a detailed microscopic analysis subsequent to the tensile tests (Fig. 6), reinforcing the classification results shown in Fig. 5b. However, it should be noted that only the most reliable trends related to AE and damage are sought in this analysis. Furthermore, no effort was made to directly associate a particular damage mode (e.g. fiber breakage) with one or more extracted AE features, as frequently attempted in the pertinent literature mentioned in this section. The AE results presented herein are however examined in comparison to related fatigue data, as described next.

4.2. Fatigue testing

Force controlled tension–tension ($R = 0.1$) fatigue tests were performed at loading rates of 2–3 Hz using a sinusoidal profile (Fig. 1c) while simultaneously recording AE, DIC and IR data. Representative stress–strain loops measured using customized DIC data recording schemes (designated with marks in Fig. 1c) are illustrated in Fig. 7a. An increase in the average maximum longitudinal strain as the fatigue process develops can be seen, which indicates changes in the overall damage condition of the tested specimen. Full field longitudinal strain distributions at specific points along a loop that corresponds to the end of the fatigue life (~99%) are shown in Fig. 7b demonstrating significant strain accumulation defined near a vertical line on the right side of the specimen, which coincided with the fractured zone.

The energy density (area inside the σ–ε loops) and residual stiffness (slope connecting the two strain extrema in the loops) are presented in Fig. 7c and d respectively as a function of normalized fatigue life and correlated to the in situ recorded cumulative AE energy. Three stages of fatigue life were identified based on these parameters and are marked with the vertical dotted lines in Fig. 7c and d. The first significant change in the slope of the AE energy curve denotes the transition from the initial stage I (0–32%) to stage II (32–84%), which is the longest out of the three. In stage II the calculated energy density gradually increases while the residual stiffness decreases, providing two additional bulk parameters to quantify the material's damage condition. The onset of stage III (>84%) was clearly identified by the sudden change in both energy density and stiffness, which is subsequently followed by a steep increase of the AE energy right before final fracture.

To further investigate the correlation between NDT data, mechanical properties and fatigue behavior, Fig. 8a shows the AE amplitude distribution in comparison with the computed average PR, while Fig. 8b presents the variation of the average x and y strains calculated from the field data presented in Fig. 8c and d as a function of fatigue life. In stage I, the initial high amplitude of AE signals associated with rapid material changes that

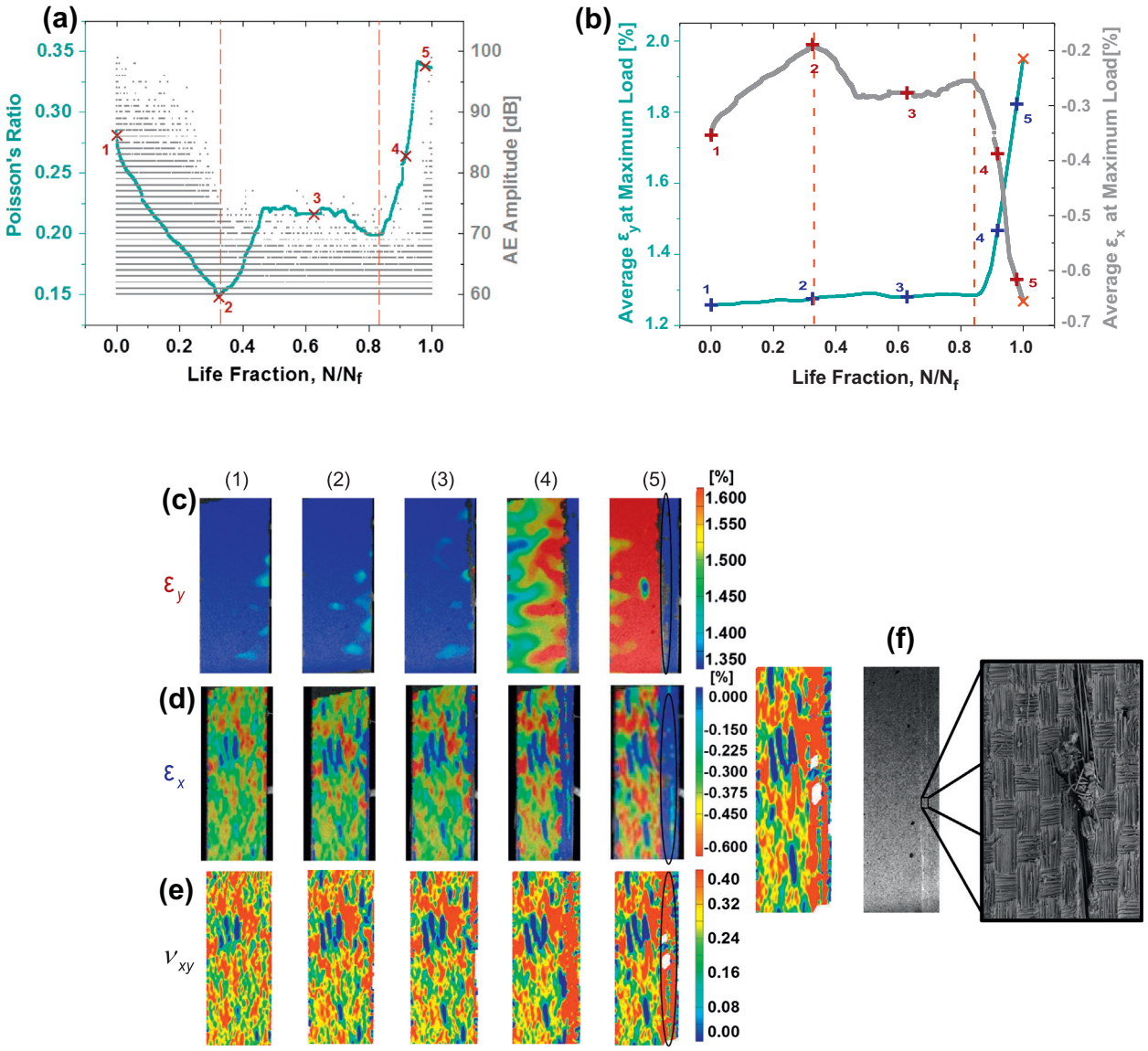

Fig. 8. (a) Poisson's ratio evolution correlated with AE amplitude and (b) maximum average longitudinal and transversal strains as a function of life fraction. Corresponding full-field strain localization maps for (c) longitudinal, (d) transversal strain and (e) Poisson's ratio. Ex situ SEM image along with optical image and Poisson's ratio fracture localization. (f) Strain map at point 5 along with DIC, and SEM optical images of fractured surface.

accommodate the imposed loading, decreases as fatigue evolves due to temporary saturation of these microstructural effects, while it is further accompanied by decreasing PR values. To investigate this trend, the full field DIC data for ε_x in Fig. 8d and PR in Fig. 8e show the appearance of localized ellipsoidal regions, in which both ε_x and ν_{xy} are significantly lower than that their neighborhood. In addition, these regions were found to be close to the distinct surface failure zone shown in Fig. 8f. The average strains values presented in Fig. 8b reveal that the calculated variations in the PR values are caused by the change in the x strains in stage I (y strains remain almost constant as also further verified by the full field data in Fig. 8c). Furthermore, a closer look at the ε_x data in Fig. 8d shows that at marked location 2 the actual failure zone starts forming from the right size of the coupon, which becomes more pronounced at locations 3–4 and can be clearly seen at location 5. Having such DIC data and motivated by the results described above, the calculation of localized Poisson ratio values shown in Fig. 8e was achieved, and demonstrated again the sensitivity of this mechanical parameter in monitoring progressive damage under fatigue loading conditions. Note that at the transition between stages II and III, both x and y strains suddenly present significant changes accompanied by the clear formation of the fracture zone in Fig. 8f, which was subsequently followed by a sharp increase of the AE amplitude as shown in Fig. 8a and an accompanying increase of the average PR values.

Further analysis of the recorded AE activity was performed by analyzing waveforms both in time and frequency domains, as shown in Fig. 9. The spectral content of the waveforms was computed using FFT. A large number of AE signals at each of the three fatigue stages was used for this analysis; however, for presentation purposes only three waveforms from each stage are presented in Fig. 9, while the remarks made correspond to the analysis of the entire data set. Specifically, although the waveform population corresponding to all identified fatigue stages comprised primarily burst-type emissions, differences in their features were identified in both time and frequency domains. Real time recorded AE signals were found to have low amplitude and short duration in stage I with their dominant frequencies centered around 150–200 kHz

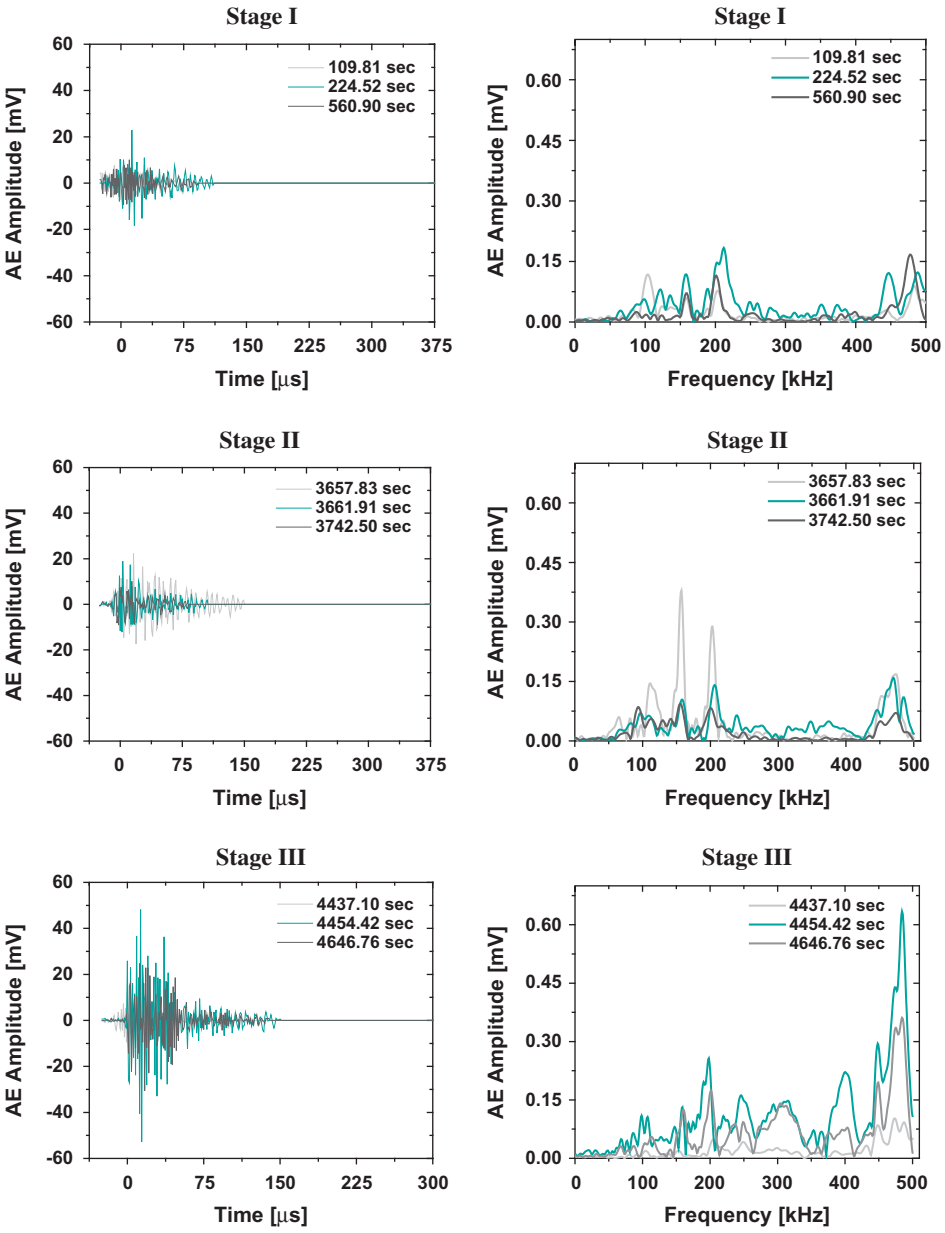

Fig. 9. (left) Selected AE waveforms and (right) their corresponding frequency content for the identified three stages of fatigue life.

and ~470 kHz. Signals extracted from stage II appeared to have relatively higher amplitude and longer duration on average and in comparison to stage I. In addition, their dominant frequency was found centered at the same frequency ranges as in stage I, but with significantly more pronounced the 150–200 kHz region compared to the 470 kHz, indicating changes (again statistically and on average) in the features of the AE emissions in this particular stage. Finally, the AE signals in stage III clearly have significantly different frequency content with a dominance of the ~470 kHz, while they additionally have much higher amplitude with respect to the AE signals associated with the previous fatigue stages. Therefore, the careful analysis of the AE population appears to yield heterogeneous features that can be used for monitoring of composite's fatigue. These findings agree well with the results presented in Fig. 5 indicating matrix and fiber failure dominated regions, which are additionally supported in this article by full field temperature and strain data (Fig. 10a and b).

Full field and average temperature and strain maps for a second fatigue sample are shown in Fig. 10 and are compared to relevant AE data. It should be noted that the results shown in this figure are for the final 1% of the fatigue life fraction (LF), where the most interesting damage evolution activity was recorded. Note also, that due to differences in the sampling rate of the DIC and IR equipment; the instances within the loops (i.e. the marked locations in Fig. 10a and b for the average longitudinal strain and temperature differential) were not always the same explaining some reported fluctuation. However, these concerns do not affect the description followed related to observed permanent damage features. Specifically, the onset of a region with pronounced heat localization is seen in Fig. 10a at the top left corner of the tested specimen and just prior to final fracture (LF = 99.3%), while no significant strain accumulation was measured in the full field data of Fig. 10b. Subsequently, at LF = 99.4% some strain accumulations at the bottom left corner of the specimen can be observed, which becomes more pronounced at LF = 99.7% and coincides with the fracture zone. Similarly, the heat localization at LF > 99.4% appears to define a distinct region near the subsequently observed fractured zone. In addition, the average temperature differential increases from

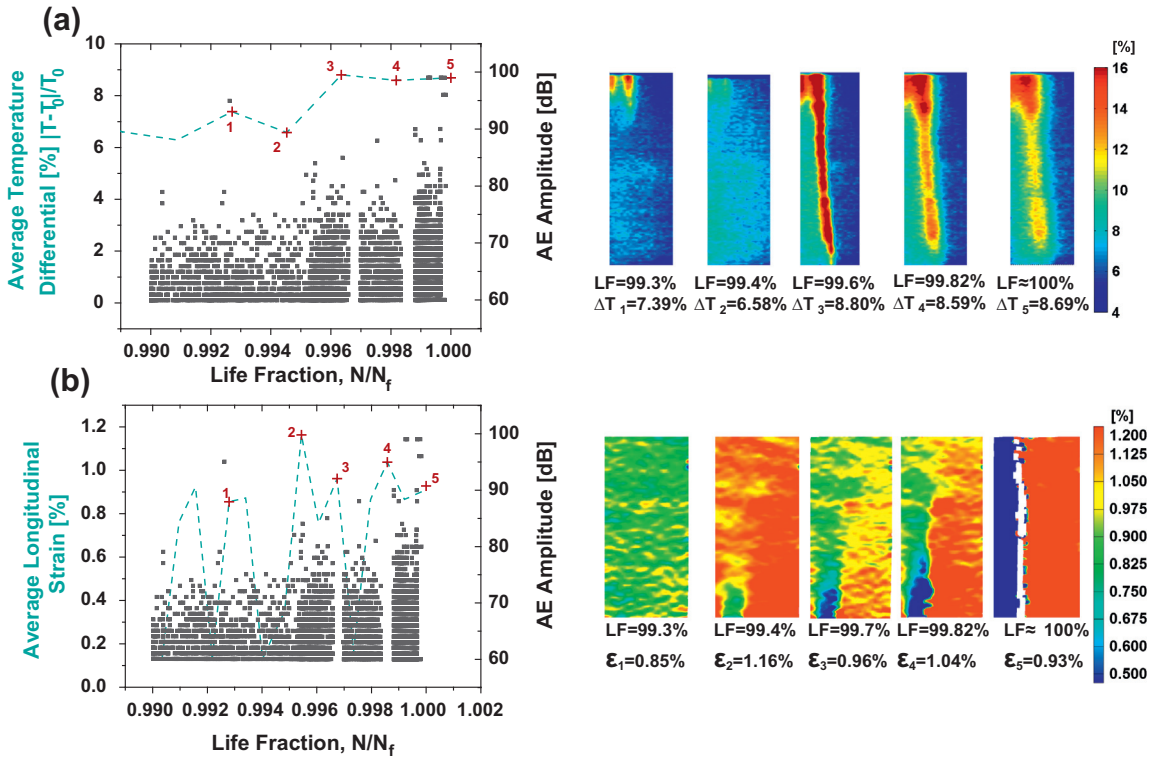

Fig. 10. (a) Average infrared thermography data correlated with AE amplitude and full field heat localization maps. (b) DIC average longitudinal strain data correlated with distribution of AE amplitude and full field strain maps.

6.58% in location 2 to 8.80% in location 3, accompanied by an increase of the corresponding AE amplitude.

5. Concluding remarks

Two main conclusions can be drawn by the results presented in this article. The first addresses the issue of NDT for damage quantification in composites. Specifically, it was repeatedly mentioned in the analysis of the results in the previous sections that for the same time/load/strain increment at which NDT or mechanical data were recorded, information evaluated by cross correlation of the independent inputs allowed both a more effective interpretation of the damage characteristics and their cross validation increasing the reliability of the monitoring strategy. The second conclusion refers to the fundamental need in understanding the mechanical and damage behavior of composites and is associated with the success of the presented hybrid NDT system to indicate the initiation and progressive development of occurring damage in both tensile and fatigue loading conditions. Rather than attempting to correlate specific features to distinct failure mechanisms, as frequently suggested when NDT methods are used in mechanical testing, this article addresses a framework for monitoring NDT changes in direct correlation to actual mechanical parameters, i.e. strains, Poisson's ratio, energy density and residual stiffness. Therefore, this article demonstrates that the careful use of available NDT technology can result in information that can feed data-driven modeling and allow the next generation of applications based on composite materials.

References

[1] Kumar S, Murthy Reddy KVVS, Kumar A, Rohini Devi G. Development and characterization of polymer–ceramic continuous fiber reinforced functionally graded composites for aerospace application. Aerospace Science and Technology. 2012.
[2] Ghasemnejad H, Occhineri L, Swift-Hook DT. Post-buckling failure in multi-delaminated composite wind turbine blade materials. Mater Des 2011;32(10):5106–12.
[3] Saheb ND, Jog JP. Natural fiber polymer composites: a review. Adv Polym Technol 1999;18(4):351–63.
[4] Phoenix SL. Modeling the statistical lifetime of glass fiber/polymer matrix composites in tension. Compos Struct 2000;48:19–29.
[5] Talreja R. Damage and fatigue in composites – a personal account. Compos Sci Technol 2008;68(13):2585–91.
[6] Fatemi A, Yang L. Cumulative fatigue damage and life prediction theories: a survey of the state of the art for homogeneous materials. Int J Fatigue 1998;20(1):9–34.
[7] Ladeveze P, LeDantec E. Damage modelling of the elementary ply for laminated composites. Composites Science and Technology. 1992;43(3):257–67.
[8] Zampaloni M, Pourboghrat F, Yankovich SA, Rodgers BN, Moore J, Drzal LT, et al. Kenaf natural fiber reinforced polypropylene composites: a discussion on manufacturing problems and solutions. Compos Part A: Appl Sci Manuf 2007;38(6):1569–80.
[9] George J, Sreekala MS, Thomas S. A review on interface modification and characterization of natural fiber reinforced plastic composites. Polym Eng Sci 2001;41(9):1471–85.
[10] Tan T, Dharan C. Cyclic hysteresis evolution as a damage parameter for notched composite laminates. J Compos Mater 2010;44(16):1977–90.
[11] Broughton WR, Gower MRL, Lodeiro MJ, Pilkington GD, Shaw RM. An experimental assessment of open-hole tension–tension fatigue behaviour of a GFRP laminate. Compos Part A: Appl Sci Manuf 2011;42(10):1310–20.
[12] Giancane S, Panella FW, Nobile R, Dattoma V. Fatigue damage evolution of fiber reinforced composites with digital image correlation analysis. Procedia Eng 2010;2(1):1307–15.
[13] Godara A, Raabe D. Influence of fiber orientation on global mechanical behavior and mesoscale strain localization in a short glass-fiber-reinforced epoxy polymer composite during tensile deformation investigated using digital image correlation. Compos Sci Technol 2007;67(11–12):2417–27.
[14] Canal LP, González C, Molina-Aldareguía JM, Segurado J, Llorca J. Application of digital image correlation at the microscale in fiber-reinforced composites. Compos Part A: Appl Sci Manuf 2011.
[15] Heinz SR, Wiggins JS. Advanced analysis of yield characteristics of composite polymer matrices using digital image correlation. SAMPE, Baltimore, MD Society for the Advancement of Material and Process Engineering; 2009.
[16] Gao X, Shao W, Ji H. Study on mechanical properties and damage behaviors of Kevlar fiber reinforced epoxy composites by digital image correlation technique under optical microscope, vol. 7657; 2010. p. 76571L.
[17] Loutas TH, Vavouliotis A, Karapappas P, Kostopoulos V. Fatigue damage monitoring in carbon fiber reinforced polymers using the acousto-ultrasonics technique. Polymer Composites 2010;31:1409–17.

[18] Bentahar M, El Guerjouma R. Monitoring progressive damage in polymer-based composite using nonlinear dynamics and acoustic emission. J Acoustical Soc Am 2009;125(1). EL39–44.
[19] Reis P, Ferreira J, Richardson M. Fatigue damage characterization by NDT in polypropylene/glass fibre composites. Appl Compos Mater 2011;18:409–19.
[20] Bourchak M, Farrow I, Bond I, Rowland C, Menan F. Acoustic emission energy as a fatigue damage parameter for CFRP composites. Int J Fatigue 2007;29(3):457–70.
[21] Marec A, Thomas JH, El Guerjouma R. Damage characterization of polymer-based composite materials: multivariable analysis and wavelet transform for clustering acoustic emission data. Mech Syst Signal Process 2008;22(6):1441–64.
[22] Wang D, Wang S, Chung DDL, Chung JH. Sensitivity of the two-dimensional electric potential/resistance method for damage monitoring in carbon fiber polymer–matrix composite. J Mater Sci 2006;41(15):4839–46.
[23] Xia ZH, Curtin WA. Damage detection via electrical resistance in CFRP composites under cyclic loading. Compos Sci Technol 2008;68(12): 2526–34.
[24] Eliopoulos EN, Philippidis TP. A progressive damage simulation algorithm for GFRP composites under cyclic loading. Part II: FE implementation and model validation. Compos Sci Technol 2011;71(5):750–7.
[25] Van Paepegem W, De Baere I, Lamkanfi E, Degrieck J. Monitoring quasi-static and cyclic fatigue damage in fibre-reinforced plastics by Poisson's ratio evolution. Int J Fatigue 2010;32(1):184–96.
[26] Kang K-W, Lim D-M, Kim J-K. Probabilistic analysis for the fatigue life of carbon/epoxy laminates. Compos Struct 2008;85(3):258–64.
[27] Allix O, Blanchard L. Mesomodeling of delamination: towards industrial applications. Compos Sci Technol 2006;66(6):731–44.
[28] Kaddour AS, Hinton MJ, Li S, Smith PA. Damage theories for fibre-reinforced polymer composites: The Third World-Wide Failure Exercise (WWFE-III). In: 16th International Conference on composite materials, 2007.
[29] Anderson TL. Fracture mechanics: fundamentals and applications. 3 ed. Boca Raton, FL: CRC; 2005.
[30] Inpil K, Mark JS, Jay HK, Vesselin S, Donglu S. A carbon nanotube strain sensor for structural health monitoring. Smart Mater Struct 2006;15(3):737.
[31] Hongo A, Kojima S, Komatsuzaki S. Applications of fiber Bragg grating sensors and high-speed interrogation techniques. Struct Control Health Monit 2005;12(3–4):269–82.
[32] Sohn H, Farrar CR, Hunter NF, Worden K. Structural health monitoring using statistical pattern recognition techniques. J Dyn Syst Meas Control 2001;123(4):706–11.
[33] Ozevin D, Greve DW, Oppenheim IJ, Pessiki SP. Resonant capacitive MEMS acoustic emission transducers. Smart Mater Struct 2006;15(6):1863.
[34] Xiukuan Z, Min L, Gangbing S, Jinwu X. Hierarchical ensemble-based data fusion for structural health monitoring. Smart Mater Struct 2010;19(4):045009.
[35] Jiang S-F, Fu C, Zhang C. A hybrid data-fusion system using modal data and probabilistic neural network for damage detection. Adv Eng Software 2011;42(6):368–74.
[36] Jiang S-F, Zhang C-M, Zhang S. Two-stage structural damage detection using fuzzy neural networks and data fusion techniques. Expert Syst Appl 2011;38(1):511–9.
[37] Rizzo P, Sorrivi E, Lanza di Scalea F, Viola E. Wavelet-based outlier analysis for guided wave structural monitoring: application to multi-wire strands. J Sound Vib 2007;307(1–2):52–68.
[38] Worden K, Manson G, Fieller NRJ. Damage detection using outlier analysis. J Sound Vib 2000;229(3):647–67.
[39] Bishop CM. Novelty detection and neural network validation. Vision Image Signal Process IEE Proc 1994;141(4):217–22.
[40] Barre S, Benzeggagh ML. On the use of acoustic emission to investigate damage mechanisms in glass-fiber-reinforced polypropylene. Compos Sci Technol 1994;52:369–76.
[41] Sause MGR, Horn S. Simulation of acoustic emission in planar carbon fiber reinforced plastic specimens. J Nondestruct Eval 2010;29:123–42.
[42] Kostopoulos V, Loutas TH, Kontsos A, Sotiriadis G, Pappas YZ. On the identification of the failure mechanisms in oxide/oxide composites using acoustic emission. NDT & E Int 2003;36(8):571–80.
[43] Pan B, Qian K, Xie H, Asundi A. Two-dimensional digital image correlation for in-plane displacement and strain measurement: a review. Meas Sci Technol 2009;20(6). 062001-062001.
[44] Cofaru C, Philips W, Van Paepegem W. Improved Newton-Raphson digital image correlation method for full-field displacement and strain calculation. Appl Opt 2010;49(33):6472–84.
[45] Shull PJ. Nondestructive evaluation: theory, techniques, and applications. CRC; 2002.
[46] Ghorbel A, Saintier N, Dhiab A. Investigation of damage evolution in short glass fibers reinforced polyamide 6,6 under tensile loading using infrared thermography. Procedia Eng 2011;10:2123–8.
[47] Toubal L, Karama M, Lorrain B. Damage evolution and infrared thermography in woven composite laminates under fatigue loading. Int J Fatigue 2006;28(12):1867–72.
[48] Meola C, Carlomagno GM, Squillace A, Prisco U, Morace RE. Analysis of composites with infrared thermography, vol. 228. Wiley-VCH Verlag; 2005. p. 273–286.
[49] Pan YP, Miller RA, Chu TP, Filip P. Detection of defects in commercial C/C composites using infrared thermography. In: SEM Annual Conference and Exposition on Experimental and Applied Mechanics 2009, June 1, 2009–June 4, 2009, vol. 1 Albuquerque, NM, United states: Society for, Experimental Mechanics; 2009. p. 199–206.
[50] Huo Y, Li H, Zhao Y, Zhang C. Study on the detectability of carbon fiber reinforced plastics composites using pulsed infrared thermography. Zhongguo Jiguang/Chin J Lasers 2010;37(Suppl. 1):277–81.
[51] Karger-Kocsis J, Harmia T, Czigany T. Comparison of the fracture and failure behavior of polypropylene composites reinforced by long glass fibers and by glass mats. Compos Sci Technol 1995;54:287–98.
[52] Hülsenberg D, Fehling P, Leutbecher T. Damage tolerant, translucent oxide fiber/glass matrix composites. Composites Part B 2008;39(2):362–73.
[53] de Groot PJ, Wijnen PAM, Janssen RBF. Real-time frequency determination of acoustic emission for different fracture mechanisms in carbon/epoxy composites. Compos Sci Technol 1995;55(4):405–12.
[54] Qi G, Wavelet-based AE. Characterization of composite materials. NDT & E Int 2000;33(3):133–44.
[55] Sause M, Horn S. Simulation of acoustic emission in planar carbon fiber reinforced plastic specimens. J Nondestruct Eval 2010;29(2):123–42.